BNL-113260-2016-JA

Dynamic Oxygen on Surface: Catalytic Intermediate and Coking Barrier in the Modeled CO2 Reforming of CH4 on Ni (111)

Kaidi Yuan, Jianqiang Zhong, Xiong Zhou, Leilei Xu, Susanna L. Bergman, Kai Wu, Guo Qin Xu, Steven L. Bernasek, Hexing Li and Wei Chen

Accepted in ACS Catalysis

June 2016

Center for Functional Nanomaterials

Brookhaven National Laboratory

U.S. Department of Energy
USDOE Office of Science,
Basic Energy Sciences

DISCLAIMER

BNL-113260-2016-JA

Dynamic Oxygen on Surface: Catalytic Intermediate and Coking Barrier in the Modeled CO_2 Reforming of CH_4 on Ni (111)

Kaidi Yuan[1,2], Jianqiang Zhong[2,8], Xiong Zhou[2,3], Leilei Xu[2], Susanna L. Bergman[5,6], Kai Wu[2,4], Guo Qin Xu[2,3], Steven L. Bernasek[5,6], Hexing Li[9], and Wei Chen[1,2,3,7]*

1 Department of Physics, National University of Singapore, 2 Science Drive 3, 117542, Singapore

2 Singapore-Peking University Research Center for a Sustainable Low-Carbon Future, 1 CREATE Way, #15-01, CREATE Tower, 138602, Singapore

3 Department of Chemistry, National University of Singapore, 3 Science Drive 3, 117543, Singapore

4 College of Chemistry and Molecular Engineering, Peking University, Beijing 100871, China

5 Science Division, Yale-NUS College, 16 College Avenue West, 138527, Singapore

6 Department of Chemistry, Princeton University, Princeton, New Jersey 08544, United States

7 National University of Singapore (Suzhou) Research Institute, 377 Linquan Street, Suzhou Industrial Park, Jiangsu 215123, China

8 Center for Functional Nanomaterials, Brookhaven National Laboratory, Upton, New York 11973, United States

9 Chinese Education Ministry Key Laboratory of Resource Chemistry, Shanghai Normal University, Shanghai 200234, China

*Corresponding Author Email Address: phycw@nus.edu.sg

Abstract

We identify Ni-O phases as important intermediates in a model dry (CO_2) reforming of methane catalyzed by Ni (111), based on results from *in operando* near ambient X-ray photoelectron spectroscopy (NAP-XPS), low energy electron diffraction (LEED) and scanning tunneling microscopy (STM). We find that under a CO_2 or CO_2-CH_4 atmosphere, the Ni-O phases exist as p(2×2) structured chemisorbed oxygen (Chem-O), epitaxial NiO (111), or oxygen-rich Ni_xO_y ($x<y$, typically Ni_2O_3), depending on the chemical potential. The growth rates of the Ni-O phases have a negative correlation with temperature from 600 K to 900 K, proving that their dynamic concentrations in the reaction are not limited by CO_2 activation, but by their thermal stability. Between 300 K and 800 K (1:1 CH_4 and CO_2 mixture), oxidation by CO_2 is dominant, resulting in a fully Ni-O covered surface. Between 800 K and 900 K, a partially oxidized Ni (111) exists which could greatly facilitate the effective conversion of CH_4. As CH_4 is activation-limited and dissociates mainly on metallic nickel, the released carbon species can quickly react with the adjacent oxygen (Ni-O phases) to form CO. After combining with carbon and releasing CO molecules, the Ni-O phases can be further regenerated through oxidation by CO_2. In this way, the Ni-O phases participate in the catalytic process, acting as an intermediate in addition to the previously reported Ni-C phases. We also reveal the carbon phobic property of the Ni-O phases, which links to the intrinsic coking resistance of the catalysts. The low dynamic coverage of

surface oxygen at higher temperatures (>900 K) is inferred to be an underlying factor causing carbon aggregation. Therefore solutions based on Ni-O stabilization are proposed in developing coking resisting catalysts.

1 Introduction

Carbon dioxide reforming of methane is a promising process for converting two major greenhouse gases to syngas (hydrogen and carbon monoxide) with a molar ratio of 1:1. Syngas can be further utilized as feedstock in the Fischer-Tropsch Reaction (H_2:CO = 2:1)[1,2] or methanol synthesis[3,4] by mixing with the products from the steam reforming of methane (H_2:CO = 3:1). Nickel has been reported as an efficient catalyst for this reaction and the rate-limiting step has been widely attributed to the activation of CH_4 [5] due to its high activation energy revealed both by experimental and theoretical work: 0.52 eV on Ni(100),[6,7] 0.74 eV on Ni (111),[8] or 0.70~0.85 eV on Ni (111).[9] It has also been reported that the observed sticking probability of CH_4 on nickel is as low as 10^{-9} at room temperature.[10-12] Whereas in the reaction, there is still a surplus of carbon from pyrolysis of CH_4 which aggregates into carbon filaments on the catalysts, causing deactivation through coking.[13-15] This problem has been suggested to arise from the lack of accessible active oxygen species during the reaction.[16]

The oxygen shortage has previously been attributed to the CO_2 activation step,[17] and some argue that unlike the activation of CH_4 which occurs on nickel, the CO_2 can only be activated on acidic/basic supports,[16,18,19] such as Al_2O_3, MgO, CaO and CeO_2.[2,19-22] The first statement has been debated since the calculated energy barrier for dissociative CO_2 adsorption on nickel is 0.40 eV lower than that of CH_4.[23] The second one has similarly been challenged by experimental work. Ruckenstein *et al* investigated the NiO-MgO system using an isotopic pulse method, identifying the oxygen in nickel as an intermediate during the reaction. They distinguished “adsorbed oxygen” and “lattice oxygen” with different reactivity to carbon species through the gas responding curve.[24] Another study by García-Diéguez *et al* determined that both CH_4 and CO_2 could be activated on the catalytic surface when separately introduced, and that the presence of CH_x can promote CO_2 activation.[25] However, direct evidence of CO_2-Ni interplay, especially *in operando* observations under reaction conditions, is still rare.

According to the Brønsted–Evans–Polany (BEP) relationship, ideal catalysts have low activation barriers for dissociative adsorption and moderate barriers for desorption.[26] If the nickel oxides function as catalytic intermediates, they are likely to desorb from the substrate under conditions employed by traditional surface science approaches (~700 ^{o}C under ultrahigh vacuum, UHV). Therefore, most of these observations are limited to low substrate temperatures.[27-29] The emergence of “near ambient pressure” (NAP) techniques have addressed some of these problems[30,31] as they operate at millibar pressures, at least 6 orders of magnitude higher than

UHV conditions. For thermally metastable species, when the total effective collisions (proportional to pressure) exceed the desorbing molecules at elevated temperatures, the products on the surface become observable using methods such as X-ray photoelectron spectroscopy (XPS). The NAP techniques also make it possible to observe intermediates only coexisting with other pressure-sensitive species.[32,33] In this way, direct observation of the competition and interaction between carbon species from CH_4 and oxygen species from CO_2 can be realized. In addition, NAP conditions can induce compositional redistribution in the solid phase, which can consequently affect the catalytic activity.[32,33]

Here we carry out studies employing near ambient pressure X-ray photoelectron spectroscopy (NAP-XPS), low energy electron diffraction (LEED) and scanning tunneling microscopy (STM) to understand the interactions of CO_2 and CO_2-CH_4 mixtures with Ni (111) at elevated pressures (millibar) and temperatures (300~900 K). It is found that nickel exhibits bi-functional catalytic behavior in the CO_2-CH_4 system by dissociating both reactants in a similar manner as previously reported for the Ru-SiO_2[19] and Mo_2C-MoO_3 systems.[34] We have observed the structural evolution of clean Ni (111) under millibar CO_2 conditions, from chemisorbed p(2×2)-O, epitaxial NiO (111), to an O-rich Ni_2O_3 top layer. The interactions between CO_2-derived Ni-O phases and CH_4 derived carbon species, as well as the regeneration of the Ni (111) have been clarified. Evidence of coking resistance originating from the Ni-O phases is also presented.

2 Experimental Section

A clean Ni (111) surface was prepared through a series of sputtering-annealing cycles. Before each experiment, both the carbon and the oxygen levels were reduced below the detection limit of XPS, and a sharp (1×1) LEED pattern was obtained. At the beginning of each experiment (high pressure cell still under UHV conditions), the valence band (VB) and the Ni $2p_{3/2}$ peak of the clean sample were measured to determine the Fermi Edge and the normalization factor respectively.

STM experiments were carried out in a multi-chamber Unisoku USM-1200 low temperature system with a base pressure below 1×10^{-10} mbar. Before each characterization, the sample was cooled down to 77 K by liquid nitrogen and stabilized for a few hours. The electrochemically etched tungsten tip was grounded, and the voltage bias was applied to the sample.

NAP-XPS experiments were performed in a multi-chamber Specs system equipped with a Mg-Al twin anode X-ray source, as well as a preparation chamber with LEED and residual gas analyzer (RGA) capabilities. The base pressure of the system was at 5×10^{-10} mbar. A second RGA was installed in the NAP lens to probe the gas composition of the NAP cell through a 300 μm nozzle. Two independent gas lines provided gas flow to the NAP cell, effectively filling the NAP cell from UHV to millibar pressure within 1~2 minutes and therefore enabling time-resolved (TR) cascade measurements. In the TR working mode, samples were first heated to a pre-set

temperature under UHV, and then dosed with reaction gas, instantly reaching the pre-set pressure. Repeated XPS measurements were carried out to record the dynamic evolution of the surface under non-equilibrium conditions. In the temperature programmed (TP) mode, the reaction gas was introduced at room temperature. The temperature was then increased in steps (typically consisting of 7 segments from 300 K to 900 K) each with a “heating” and a "dwelling” period. NAP-XPS measurements were conducted at each temperature after sufficient dwelling time, in order to reach surface conditions close to equilibrium.

3 Results and Discussion

3.1 Structural characterization of CO_2-derived Ni-O phases by STM and LEED: p(2×2) Chem-O and epitaxial NiO (111)

The structures of CO_2-derived Ni-O phases were characterized by STM and/or LEED after a separate treatment of 100 L (Langmuir) CO_2 exposure at 1.3×10^{-6} mbar, 300 K; and another series of consecutive treatments of (1) 0.4 mbar CO_2 exposure at 600~700 K for 1 hour; (2) mild sputtering (500 V instead of regular 1500 V, 5min) and flashing in UHV at 773 K (1 min) of the sample in (1); and (3) further annealing the sample in (2) in UHV at 973 K. Similar to the O_2-derived Ni-O phases,[35-37] both the p(2x2) chemisorbed structure, and epitaxial NiO (111) were observed.

Figure 1 (a) shows an STM image after exposing the clean Ni (111) to 100 L CO_2 at room temperature. An ordered surface structure is observed with the unit cell marked by a white diamond (0.51±0.03 nm in length). Considering the distance of 0.249 nm between adjacent atoms in Ni (111), this pattern is consistent with the p(2×2) structure. For comparison, Figure 1 (b) shows the surface after 100 L dosing of O_2 at 300 K and subsequent annealing in UHV at 773 K. The unit cell also has the p(2x2) structure with a measured length of 0.49±0.04 nm. In Figure 1 (c), the Ni (111) was first exposed to 0.4 mbar CO_2 for 1 hour at 700 K to form NiO (as evidenced by LEED measurements), and then transferred to the STM chamber. To eliminate the effects of air contamination during the transfer, the sample was cleaned by mild sputtering (500 V, 5min) and UHV annealing (773 K, 1 min) before imaging. The same p(2x2) pattern can be seen, and the defects (red dots) originating from thermal treatment are similarly distributed. Further heating the sample at elevated temperature (973 K) in UHV for 10 min resulted in near complete decomposition of the oxides, leaving a few oxide-phase islands, still maintaining the local p(2×2)-O structure on the bare Ni (111), as shown in Figure 1 (d).

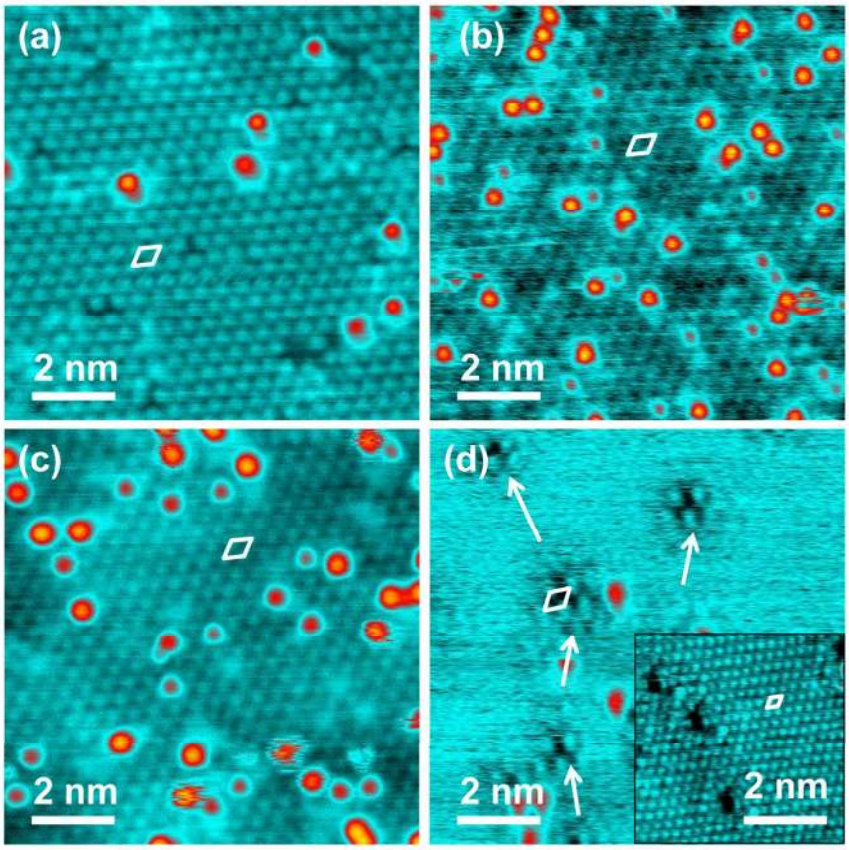

Figure 1. STM images of Ni-O(2×2) structures formed on Ni (111) after (a) exposing to 100 L CO_2 at room temperature; (b) after exposing to 100 L O_2 at RT followed by annealing at 773 K; (c) after exposing to 0.4 mbar CO_2 for 1 hour at 700 K, transferred in air, and cleaned by sputtering and annealing; and (d) after further annealing the sample corresponds to panel (c) at 973 K, leaving residual Chem-O islands dispersed on the flat surface [insert illustrates the same surface showing the Ni (111) lattice]. The unit cells were marked by diamonds, and measured as (a) 0.51±0.03 nm, (b) 0.49±0.04 nm, (c) 0.48±0.03 nm, (d) 0.49±0.04 nm for the residual islands, and 0.25±0.02 nm for the insert. The bias voltages and tunneling currents were (a) -0.2 V, 0.1 nA; (b) -0.05 V, 0.5 nA; (c) -0.2 V, 0.1 nA; (d) -0.1 V, 0.2 nA, and the insert -0.1 V, 10 nA.

Figure 2 (a) shows the LEED pattern of clean Ni (111) using a beam energy of 70 eV. Sharp diffraction spots in six-fold symmetry can be seen. Figure 2 (b) shows the diffraction pattern of the Ni (111) sample after exposure to 0.4 mbar CO_2 at 700 K for 30 min. The beam energy and position were kept constant. Again the pattern shows the six-fold symmetry, epitaxial to that of Ni (111) as noted by the red dashed hexagon. By carefully measuring the diffraction lattices of the clean and the CO_2-exposed samples, a ratio of 1.2 was obtained. This is consistent with the ratio between the sodium chloride structured NiO (111) (a=0.418 nm) and the face-centered cubic Ni (111) (a=0.3524 nm). This ratio was also obtained when exposing the clean surface to 20~30 L O_2, see Figure S1, further proving the similarity between CO_2-derived NiO and O_2-derived NiO. It is noted that the NiO (111) diffraction patterns of both origins are blurred. We attribute this to an amorphous Ni_2O_3 top layer as revealed by XPS in Figure 3 (a), and the small grain size of the formed oxides (less than 5 nm) as similarly observed by Butcher *et al* in

their Pt-O_2 system.[38] Although the sodium chloride structured NiO is stable under an oxidizing atmosphere, its oxygen can be released from the surface if heated in UHV or reducing atmosphere. Figure 2 (c, d) show that after UHV annealing at 700 K, the sodium chloride structured NiO (111) transformed into a p(2×2) structure. Using a beam energy of 70 eV, another set of diffraction patterns with 30^o rotation could be identified (yellow hexagon). But this pattern became less significant when increasing the beam energy to 110 eV. As the beam of higher energy has larger penetration depth, it is inferred that the rotated pattern originates from decomposition of the topmost Ni_2O_3 layer. Compared with stoichiometric NiO, the p(2×2) Chem-O structure has less dense oxygen concentration on the surface (4:1 nickel to oxygen atomic ratio) in a reducing environment, in agreement with the results by STM.

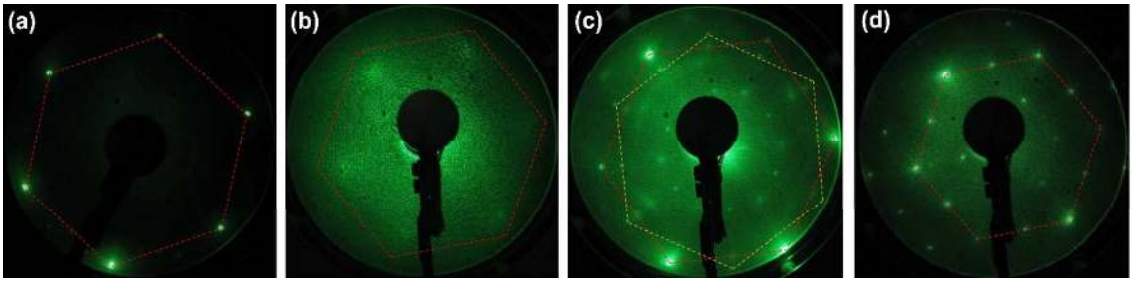

Figure 2. LEED patterns of (a) clean Ni (111), beam energy 70 eV ; (b) after exposure to 0.4 mbar CO_2 at 600 K for 30 min, beam energy 70 eV, showing a shrinkage of the diffraction lattice consistent with epitaxial NiO (111) on Ni (111); and (c, d) the condition of (b) after UHV annealing, using 70 eV and 110 eV beams, showing the transition from NiO (111) to the p(2x2) Chem-O structure. The hexagons in red dashed lines denote the unit diffraction lattice of clean Ni (111), and that in yellow dashed lines denotes a rotated pattern.

Both the STM and LEED results demonstrate that the p(2×2) structured Chem-O on Ni (111) can be obtained either after the initial exposure of a clean sample, or after moderate annealing of NiO/Ni_2O_3 in UHV. As CO_2 is less reactive than O_2 at room temperature, 100 L CO_2 dosing resulted in only partially covered Chem-O while less than 50 L O_2 dosage achieved full coverage.[39-43] It was also observed that when the dosing was carried out at 973 K (at 1.3×10^{-6} mbar), oxygen could rarely be found even after 1000 L CO_2 exposure, as shown in Figure S2. This illustrates the thermally unstable nature of the Chem-O phase. The dissociative adsorption of CO_2 results in *CO and *O on the clean Ni surface, with 0.72 eV energy released.[44] Although the desorption of *CO is believed to be a strongly endothermic process on clean metal surfaces,[19,59] in oxygen saturated nickel however, the desorption energy is reduced by about 0.17 eV due to repulsive interactions between the surface oxygen and *CO. As such, release of CO is possible at room temperature.[45] This explains why the dominantly observed structure is the oxide phase rather than the *CO in Figure 1.

3.2 Temperature-programmed NAP-XPS characterization of CO_2-Ni (111) interactions: identification of NiO and Ni_2O_3 phases

The interaction between CO_2 and Ni (111) was studied by temperature-programmed NAP-XPS under 4.0×10^{-1} mbar CO_2 from 300 K to 900 K. At each temperature, the system was allowed at least 2 hours to ensure equilibrium conditions. In Figure 3 (a), three O 1s peaks are clearly identified with binding energies of 536.8 eV for gas phase CO_2, 531.5 eV for Ni_2O_3,[46] and 529.5 eV for NiO.[47,48] The latter two peaks are fitted by the red and green curves respectively, and their areas are illustrated in Figure 3 (d). The Ni_2O_3 content remains stable below 600 K but slowly decreases at higher temperatures, while the NiO keeps increasing until 900 K. This is in agreement with previous reports showing that the NiO (111) / Ni (111) interface is more stable.[37,49,50] In Figure 3 (b), the C 1s peak at 289.2 eV is attributed to the adsorbed $*CO_2^{\delta-}$,[51] and that at around 293 eV to gas phase CO_2 affected by the surface work function.[52-56] The peak area ratio of $*CO_2^{\delta-}/CO_{2,gas}$ is summarized in Figure 3 (e). Similarly to the O 1s case, there is also a gap present between 600 K and 700 K. Figure 3 (c) shows the evolution of Ni $2p_{3/2}$ peak. More metallic nickel was converted to nickel oxides with increasing temperature, as shown by the disappearance of the metallic peak at 852.4 eV[57] and the emerging of the Ni^{2+} peak at 854.4 eV.[48] The Ni^{3+} peak (~856.0 eV) was weak compared to the Ni^0 and Ni^{2+}, implying that the Ni_2O_3 existed as a single layered interface between the solid and gas phases. The relationship between the thickness of the NiO and the remaining Ni^0 peak area (normalized by the area of clean nickel) was estimated using “oxides (NiO, CuO, and CoO) on Ni” models, and the SESSA 2.0 software. The result was plotted in Figure 3 (f). According to an exponential decay estimation, under a 1486.6 eV incident beam, the inelastic mean free path (IMFP) for Ni^0 2p (λ_{Ni}) is 1 nm (the Ni peak area decays by 1/e with 1.0 nm NiO on top), and that for O 1s (λ_O) is 2 nm.

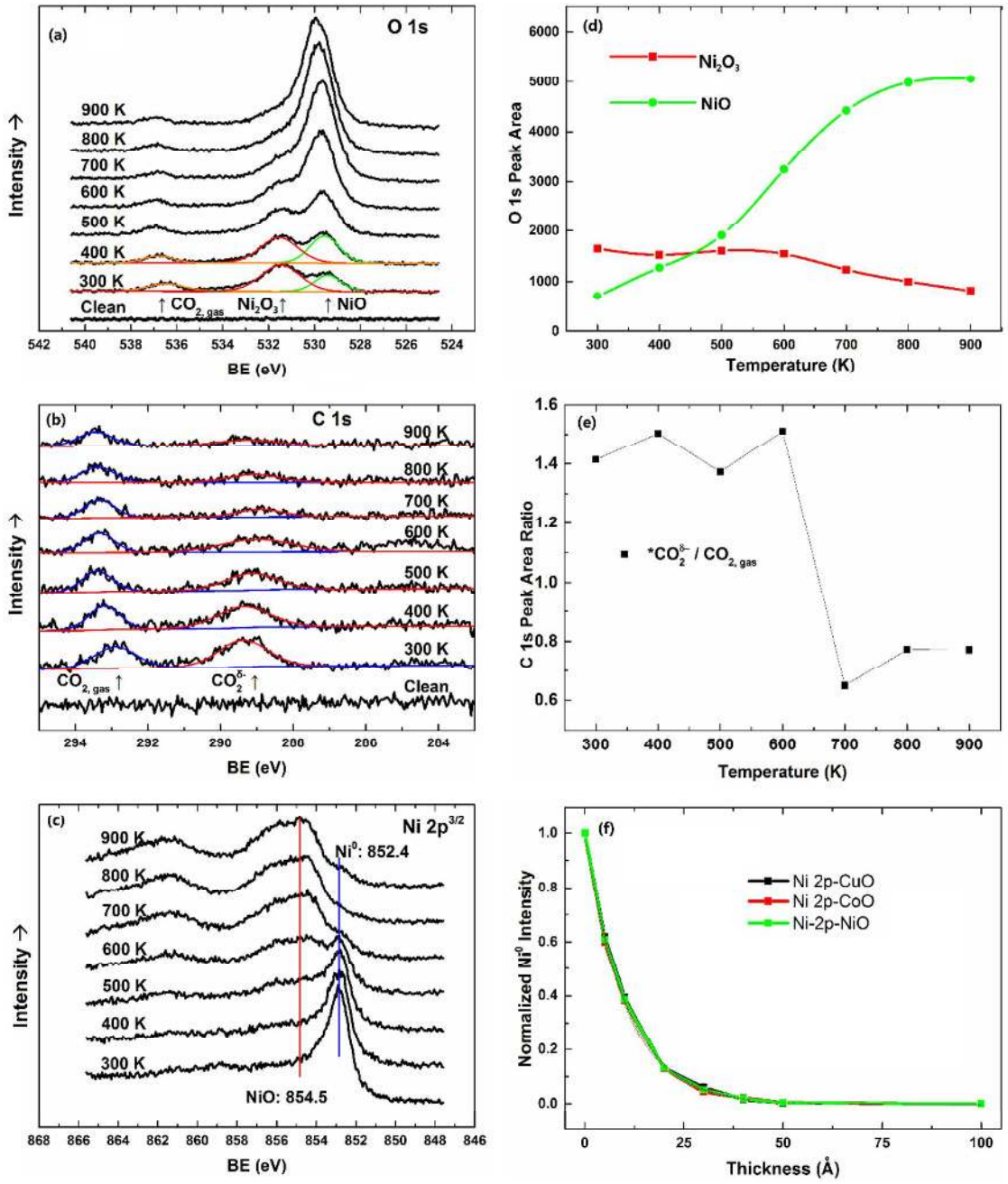

Figure 3. Temperature-programmed NAP-XPS under 0.4 mbar CO_2 from 300 K to 900 K. (a-c) O 1s, C 1s and Ni $2p_{3/2}$ peaks. (d) Fitted O 1s areas by NiO (green) and Ni_2O_3 (red). (e) C 1s area ratio of $*CO_2^{\delta-}/CO_{2,gas}$. (f) SESSA 2.0 simulated Ni^0 2p intensity (normalized) from nickel substrates covered by CuO, CoO, and NiO with varying thicknesses.

Two activation mechanisms for CO_2 on Ni (111) have been reported: dissociative adsorption (Eq. 1),[18,58] and non-dissociative adsorption through charge transfer and molecular bending (Eq. 2.): [38]

$CO_2 \rightarrow *CO + *O$ (Equation 1)

$CO_2 + \delta\, e^- \rightarrow *CO_2^{\delta-}$. (Equation 2)

In the dissociative mechanism, the dissociated products form Chem-O and *CO adsorbate with the C 1s peak located around 286 eV.[34,59] In the non-dissociative mechanism, partial electron transfers from Ni(111) to CO_2 to form the negatively charged $*CO_2^{\delta-}$ adsorbate with the characteristic C 1s peak at ~288.5 eV.[59,60] In Figure 3, although the existence of the Ni-O phase confirms the dissociation of CO_2 at even room temperature, the dominant carbon adsorbate is the $*CO_2^{\delta-}$ rather than *CO. This could be explained by the adsorption-desorption equilibrium. It is noted that the rate of dissociative adsorption is much lower than the collision of CO_2 molecules (>10^5 collisions per second at mbar pressure); whereas, the low *CO yielding rate cannot exceed the desorption of *CO in the circumstance of low CO base pressure (< 1×10^{-9} mbar) and weakened bond between *CO and Ni-O phase;[45] as a result, the major carbon species on the surface is $*CO_2^{\delta-}$. A similar effect was also reported in the case of a CO/H_2O mixture.[59] Here, the adsorbate on Cu (111) was mainly in the form of *CO, while on CeO_x / Cu (111) the $*CO_2^{\delta-}$ was found to dominate on the surface.

3.3 Temperature-programmed NAP-XPS characterization under a CH_4 and CO_2 atmosphere: from fully carbon-covered Ni, fully oxide-covered Ni, to partially (C, O)-covered Ni

To study the gas-nickel interface under conditions resembling the actual dry reforming reaction, a series of temperature-programmed NAP-XPS experiments were carried out in a gas mixture (0.4 mbar CH_4 and 0.4 mbar CO_2) from 300 K to 900 K. In Figure 4 (a), the O 1s peaks belonging to gas phase CO_2 locate near 537.0 eV. The peak positions have been affected by the change of the surface work function due to oxidation and reduction. The peaks at 531.5 eV for Ni_2O_3 and 529.7 eV for NiO are not observed at 300 K. This is due to the passivation by carbon from pyrolysis of CH_4 on Ni (111) and will be explained later. The Ni-O phase first appears at 400 K, and increases until 700 K. At 800 K, the intensity decreases and the peak center shifts to higher binding energy by ~0.3 eV compared to the initial value. At 900 K, neither of the two peaks (NiO and Ni_2O_3) remains, as highlighted in green. In Figure 4 (b), the C 1s gas phase peaks for both CO_2 and CH_4 exhibit similar trends as the O 1s region: positive shifts between 400 K and 800 K and recovery at 900 K. In the operation, CH_4 was introduced before CO_2 and the red spectrum for "CH_4 only" has a characteristic peak at 283.7 eV. This peak can be attributed to the partially dissociated *CH with one remaining hydrogen[27]. It remains after the introduction of CO_2 at 300 K, but disappears at higher temperatures. In Figure 4 (c), the Ni^0 peak turns weak between 400 K and 800 K due to surface oxidation, but recovers to the original intensity at 900 K, indicating that the surface oxides have been completely reduced.

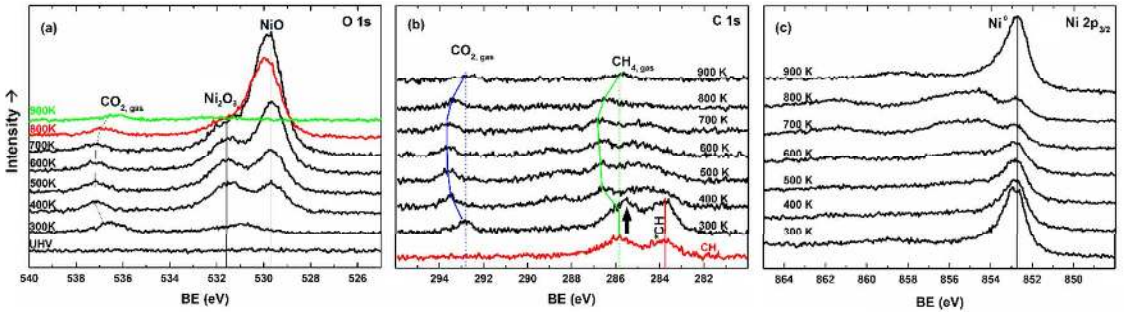

Figure 4. Temperature-programmed XP spectra of (a) O 1s, (b) C 1s and (c) Ni $2p_{3/2}$ under 0.4 mbar CH_4 and 0.4 mbar CO_2.

Compared to the pure CO_2 case (Figure 3), apart from the obvious difference in the high temperature (800-900 K) region, two additional features at 300 K can be observed under the mixed gas atmosphere. The first feature is due to the *CH-induced surface passivation. Since CH_4 was dosed first, the Ni (111) surface was covered by *CH species from CH_4 pyrolysis. This carbon layer blocked the Ni-O formation, as indicated by the absence of the characteristic O 1s peak at 529.5 eV. Such passivation on nickel has been widely reported, with the carbon clusters varied from CH_x, graphite carbon to graphene.[61-64] The second feature lies in the difference between C 1s spectra labeled "CH_4" (only CH_4 at 300 K) and "300 K" (CO_2+CH_4 at 300 K). After introducing the CO_2, although the *CH species were not removed, a new C 1s peak appeared at 285.7 eV as pointed out by the arrow in Figure 4 (b), indicating the interaction between CO_2-derived and CH_4-derived intermediates. The peak is attributed to an oxidized form of the *CH species, which were completely consumed from 400 K onward, owing to the highly active CO_2-nickel interface.

3.4 Time-resolved NAP-XPS characterization of the Gas-Ni interface: revealing the metastable nature of the Ni-O phases under CO_2 and CO_2/CH_4 atmospheres

In order to study the dynamic evolution of the Ni-O phases affected by temperature and pressure, time-resolved (TR) NAP-XPS experiments were carried out by monitoring the O 1s peaks in intervals of several minutes. Normalized peak areas were plotted against time. Figure S3 demonstrates a continuous TR experiment with three independent variables: substrate temperature as well as the partial pressures of CO_2 and CH_4. Segments labelled from "A" to "R" represent specific combinations of parameters. For clarity, two typical data sets were selected and shown in the main text.

Figure 5 (a) shows the time-resolved oxidation of Ni (111) under pure CO_2 from 600 K to 900 K. It is discovered that the oxidation rate is temperature-sensitive with a strong negative correlation. At 900 K, the oxygen level remains close to zero with respect to time. Upon slightly

reducing the temperature to 880 K, however, the increase of oxygen emerges. Further reducing the temperature from 850 K to 750 K results in an even higher growth rate. At temperatures between 750 K and 600 K, the curves exhibit an almost instant step-up in the initial stage, followed by a near-saturation stage. Figure 5 (b) illustrates the reduction of the Ni-O phase under 0.3 mbar CH_4. The sample was from the TR-CO_2 treatment at 600 K in Figure 5 (a). During the initial 3 hours, the system was kept at 600 K, but only a slight decrease in the oxygen was observed, showing that the Ni-O phases remained stable at this temperature even in a reducing atmosphere. By increasing the temperature to ~800 K, the oxygen level quickly fell below the detection limit of XPS.

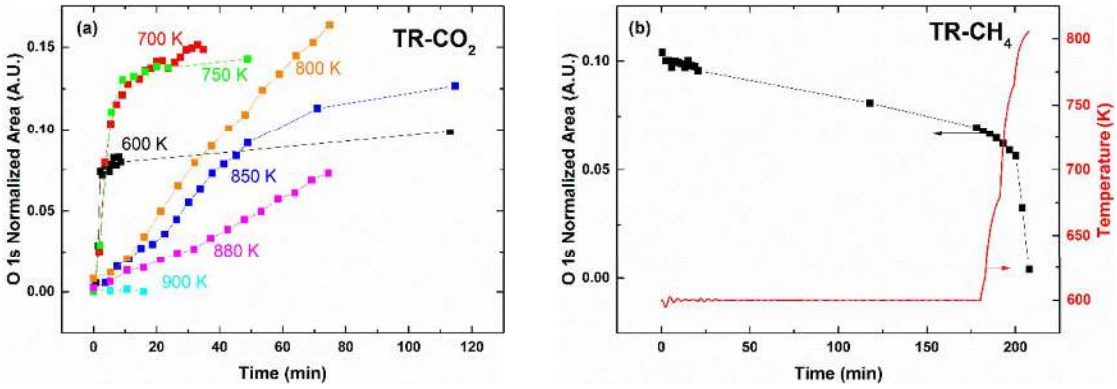

Figure 5. Time-resolved NAP-XPS showing the O 1s peak evolution. (a) Accumulation of oxygen under 0.4 mbar CO_2 at varying temperatures; (b) the reduction of the Ni-O phase under 0.3 mbar CH_4, prepared from the oxidation in (a) at 600 K.

The combination of TP and TR measurements provides a deeper understanding of the model catalysis system. The “instant” step-up of oxygen in pure CO_2 below 750 K [Figure 5 (a)], the prevailing oxidation in the CO_2-CH_4 mixture below 700 K (Figure 4), and the poor reducing ability of pure CH_4 below 700 K [Figure 5 (b)] demonstrate that the activation of CO_2 is not a limiting factor compared with CH_4 activation. The energy barrier for CO_2 dissociation to CO* and O* is not only lower than that of CH_4 dissociation, but also the release/diffuse of O* on the Ni surface. Unlike aluminum and magnesium that being oxidized in a nearly irreversible manner, the reversibility of the Ni-NiO transition is a fundamental property of a catalyst operating in an atmosphere consisting of oxidizing and reducing gases. *In vacuum* decomposition has been reported by Maglia *et al* for single crystal NiO at temperatures around 773 K,[65] and by Jang *et al* for thin film NiO at 673 K.[66] In the dry reforming reaction, high temperatures (≥800 K) are mainly used to mobilize the O*, as well as to activate the dissociation of CH_4 molecules. The released O* from the Ni-O reacts with carbon radicals from CH_4, acting as a catalytic intermediate because the adsorbed thermal energy here is much lower than that required for directly breaking the C=O bond in CO_2.

3.5 Carbon-phobic properties of the Ni-O phases and their role in coking resistance

Coking is a major problem in catalysis caused by carbon aggregation on the surface. The carbon originates from either cracked CH_4 species,[62] or CO disproportionation through the Boudouard Reaction.[16,66,67] As the chemical inertness of the carbon species is related to the bonding nature and size of the clusters, prevention of the spillover of carbon to form sp2 and sp3 networks is paramount. The intrinsic coking resistance of the partially oxidized nickel is based on three major mechanisms: the low CH_4 cracking rate on Ni-O phases controls carbon (C_1) supply, the released oxygen consumes the formed C_1, and the surface oxygen blocks the diffusion of C_1 and therefore reduces opportunity for C_2 (and C_n) formation. In macroscopy, such surface will behave as carbon phobic.

To compare the carbon philic/phobic properties of the Ni and Ni-O phases, a pair of titration experiments were carried out at 700 K at which the activated CH_4 is significant while the NiO could remain for hours. In Figure 6 (a), the clean Ni (111) was first dosed with 0.12 mbar CH_4. In the C 1s spectrum, the gas phase peak and the peak for Ni_xC (BE = 283.6 eV, attributed to a mixture of Ni_2C and Ni_3C[68,69]) can be clearly identified, showing carbon philic property of the metal surface. After finishing the XPS scan, the cell was filled by another 0.05 mbar CO_2. Although the mixture was CH_4 dominant (70% v/v), the CH_4-derived Ni_xC phase still disappeared. In a parallel experiment (Figure 6 (b)), the Ni (111) was first exposed to 0.4 mbar CO_2 to form a Ni-O layer on the surface. The cell was then evacuated to UHV to avoid possible Eley-Rideal type reaction between CO_2 and Ni_xC. Subsequently, pure CH_4 at 0.12 mbar was introduced to the cell. In contrast to the metallic surface, carbon adsorbates can rarely be found in the spectrum (except for the gas phase peak of CH_4 which disappeared after CH_4 evacuation), indicating that the oxygen covered surface is carbon phobic.

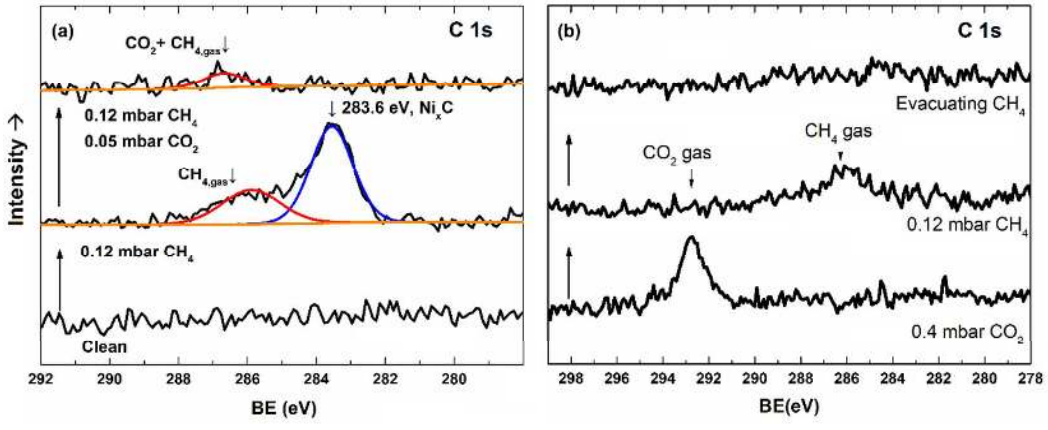

Figure 6. Titration experiments at 700 K with varying gas dosing sequences. In (a), the Ni (111) was first exposed to 0.12 mbar CH_4 at 700 K and Ni_xC clusters were formed; after adding another 0.05 mbar CO_2, the Ni_xC phase

disappeared. In (b), the Ni (111) was first exposed to 0.4 mbar CO_2 at 700 K to form a NiO surface; after evacuating the CO_2 and adding 0.12 mbar CH_4, no carbon deposition was observed on the oxidized surface except for the gas phase CH_4 peak, which disappeared after evacuating CH_4.

Due to the metastable and carbon phobic nature of the Ni-O phase, by tuning its dynamic concentration using temperature and partial pressure, the amount of surface carbon is able to be controlled. Ideally, a Ni surface partially covered by surface oxides could maximize the relative collision rate of CH_4,[5,70] and partition catalysts into smaller ensembles similar to bi-metallic alloying and potassium doping[71] which show higher resistance to coking. In this way, a correlation between surface oxygen and coking resistance can be established. A similar link can also be found in some noble metals like Ru,[72,73] Pd,[70,74] Ir[75] and Pt[38,76] that show high coking resistance in the dry reforming reaction[5,18,41,16,77] However, the authors had not yet related the coking performance to the known surface oxides of these metals in the reaction ambient.

At current dry reforming temperatures (1000 ~ 1274 K),[18] the role of intrinsic coking resistance from the Ni-O phase on single crystal Ni (111) is suppressed. On one hand, the lifetime of the surface oxygen decreases; on the other hand, a larger portion of CH_4 molecules are thermally dissociated; both contributing to the spillover of carbon species. Therefore the stabilization of the Ni-O phase under operating temperatures becomes an open question. One possible method is to reduce the catalyst into nanoparticles and confine them to mesoporous structures, as the oxides become more stable due to the size effect.[78,79] In addition, diffusion of oxygen through the bulk is more significant on the nano-scale, enhancing another oxygen supply channel, i.e. the migration from support to surface. Therefore the oxygen activated in the support can also make a positive contribution to the metal surface.

Conclusion

Dissociation of CO_2 on the Ni (111) surface at temperatures between 300 and 900 K has been observed *in operando* by NAP-XPS. CO_2 quickly reacts with clean nickel and forms various Ni-O phases even at room temperature: initially the p(2×2) structured Chem-O, followed by epitaxial NiO (111) with a sodium chloride structure and finally an oxygen enriched surface layer of Ni_2O_3 under oxidative potential. For the Ni-O phases, we discover that their accumulation rate under CO_2 has a negative correlation with temperature, revealing that the dynamic oxygen concentration is not limited by CO_2 activation, but the thermal decomposition of the Ni-O phases. The Ni-O phases exhibit carbon phobic properties due to repulsive force to *CO adsorbate and lower C-H bond scission rate than metallic Ni, showing intrinsic coking resistance. The releasing of oxygen from both NiO and Chem-O is verified upon heating, acting as an intermediate to react with the carbon species from dissociated CH_4. Therefore it is inferred that maintaining a certain level of surface oxygen can optimize the utilization of CH_4 and improve the coking resistance. There are already reports on the catalytic improvement from partially oxidized transition metals

(Fe,[80] Co,[81] Ni,[82] Pd,[83,84] and Pt[76]), with oxygen originating from either atmosphere or reactive supports. From the perspective of surface oxygen, it is interestingly found that many of current coking prevention methods such as size reduction,[5] alkaline ion doping,[71] use of reducing supports (CeO_x and TiO_x)[60] and noble metals alloying, are increasing the surface oxygen concentration of the active metal in essence.

Acknowledgements

The authors acknowledge the financial support from Singapore MOE grant R143-000-542-112, Singapore National Research Foundation CREATE-SPURc program R-143-001-205-592, NFSC program (21573156), and Academia-Industry Collaborative Innovation Foundation 20121G00421 and BY2014139 from Jiangsu Science and Technology Department.

References

(1) Dry, M. E. *Catalysis Today* **2002**, *71*, 227.

(2) Olah, G. A.; Goeppert, A.; Czaun, M.; Prakash, G. K. S. *Journal of the American Chemical Society* **2012**, *135*, 648.

(3) Olah, G. A.; Goeppert, A.; Czaun, M.; Mathew, T.; May, R. B.; Prakash, G. K. S. *Journal of the American Chemical Society* **2015**, *137*, 8720.

(4) Goeppert, A.; Czaun, M.; Jones, J.-P.; Surya Prakash, G. K.; Olah, G. A. *Chemical Society Reviews* **2014**, *43*, 7995.

(5) Chin, Y.-H.; Buda, C.; Neurock, M.; Iglesia, E. *Journal of the American Chemical Society* **2011**, *133*, 15958.

(6) Chorkendorff, I.; Alstrup, I.; Ullmann, S. *Surface Science* **1990**, *227*, 291.

(7) Holmblad, P. M.; Wambach, J.; Chorkendorff, I. *The Journal of Chemical Physics* **1995**, *102*, 8255.

(8) Yang, H.; Whitten, J. L. *The Journal of Chemical Physics* **1992**, *96*, 5529.

(9) Watwe, R. M.; Bengaard, H. S.; Rostrup-Nielsen, J. R.; Dumesic, J. A.; Nørskov, J. K. *Journal of Catalysis* **2000**, *189*, 16.

(10) Bengaard, H. S.; Alstrup, I.; Chorkendorff, I.; Ullmann, S.; Rostrup-Nielsen, J. R.; Nørskov, J. K. *Journal of Catalysis* **1999**, *187*, 238.

(11) Abild-Pedersen, F.; Lytken, O.; Engbæk, J.; Nielsen, G.; Chorkendorff, I.; Nørskov, J. K. *Surface Science* **2005**, *590*, 127.

(12) Schouten, F. C.; Gijzeman, O. L. J.; Bootsma, G. A. *Surface Science* **1979**, *87*, 1.

(13) Snoeck, J. W.; Froment, G. F.; Fowles, M. *Journal of Catalysis* **1997**, *169*, 250.

(14) Li, K.; Jiao, M.; Wang, Y.; Wu, Z. *Surface Science* **2013**, *617*, 149.

(15) Xu, L.; Song, H.; Chou, L. *Catalysis Science & Technology* **2011**, *1*, 1032.

(16) Pakhare, D.; Spivey, J. *Chemical Society Reviews* **2014**, *43*, 7813.

(17) Kawi, S.; Kathiraser, Y.; Ni, J.; Oemar, U.; Li, Z.; Saw, E. T. *ChemSusChem* **2015**, *8*, 3556.

(18) Nagaoka, K.; Seshan, K.; Lercher, J.; Aika, K.-i. *Catalysis Letters* **2000**, *70*, 109.

(19) Ferreira-Aparicio, P.; Rodríguez-Ramos, I.; Anderson, J. A.; Guerrero-Ruiz, A. *Applied Catalysis A: General* **2000**, *202*, 183.

(20) Xu, L.; Song, H.; Chou, L. *ACS Catalysis* **2012**, *2*, 1331.

(21) Xu, L.; Song, H.; Chou, L. *Applied Catalysis B: Environmental* **2011**, *108–109*, 177.

(22) Xu, M.; Iglesia, E. *The Journal of Physical Chemistry B* **1998**, *102*, 961.

(23) Wang, S.-G.; Cao, D.-B.; Li, Y.-W.; Wang, J.; Jiao, H. *The Journal of Physical Chemistry B* **2006**, *110*, 9976.

(24) Ruckenstein, E.; Hu, Y. *Catalysis Letters* **1998**, *51*, 183.

(25) García-Diéguez, M.; Pieta, I. S.; Herrera, M. C.; Larrubia, M. A.; Malpartida, I.; Alemany, L. J. *Catalysis Today* **2010**, *149*, 380.

(26) Norskov, J. K.; Bligaard, T.; Hvolbaek, B.; Abild-Pedersen, F.; Chorkendorff, I.; Christensen, C. H. *Chemical Society Reviews* **2008**, *37*, 2163.

(27) Larciprete, R.; Goldoni, A.; Grošo, A.; Lizzit, S.; Paolucci, G. *Surface Science* **2001**, *482–485, Part 1*, 134.

(28) Vesselli, E.; Rogatis, L. D.; Ding, X.; Baraldi, A.; Savio, L.; Vattuone, L.; Rocca, M.; Fornasiero, P.; Peressi, M.; Baldereschi, A.; Rosei, R.; Comelli, G. *Journal of the American Chemical Society* **2008**, *130*, 11417.

(29) Feng, X.; Cerdá, J. I.; Salmeron, M. *The Journal of Physical Chemistry Letters* **2015**, *6*, 1780.

(30) Frank Ogletree, D.; Bluhm, H.; Hebenstreit, E. D.; Salmeron, M. *Nuclear Instruments and Methods in Physics Research Section A: Accelerators, Spectrometers, Detectors and Associated Equipment* **2009**, *601*, 151.

(31) Tao, F.; Grass, M. E.; Zhang, Y.; Butcher, D. R.; Renzas, J. R.; Liu, Z.; Chung, J. Y.; Mun, B. S.; Salmeron, M.; Somorjai, G. A. *Science* **2008**, *322*, 932.

(32) Hansen, P. L.; Wagner, J. B.; Helveg, S.; Rostrup-Nielsen, J. R.; Clausen, B. S.; Topsøe, H. *Science* **2002**, *295*, 2053.

(33) Tan, K.; Zuluaga, S.; Gong, Q.; Gao, Y.; Nijem, N.; Li, J.; Thonhauser, T.; Chabal, Y. J. *Chemistry of Materials* **2015**, *27*, 2203.

(34) Porosoff, M. D.; Yang, X.; Boscoboinik, J. A.; Chen, J. G. *Angewandte Chemie International Edition* **2014**, *53*, 6705.

(35) Narusawa, T.; Gibson, W. M.; Törnqvist, E. *Surface Science* **1982**, *114*, 331.

(36) Tyuliev, G. T.; Kostov, K. L. *Physical Review B* **1999**, *60*, 2900.

(37) Hildebrandt, S.; Hagendorf, C.; Doege, T.; Jeckstiess, C.; Kulla, R.; Neddermeyer, H.; Uttich, T. *Journal of Vacuum Science & Technology A* **2000**, *18*, 1010.

(38) Butcher, D. R.; Grass, M. E.; Zeng, Z.; Aksoy, F.; Bluhm, H.; Li, W.-X.; Mun, B. S.; Somorjai, G. A.; Liu, Z. *Journal of the American Chemical Society* **2011**, *133*, 20319.

(39) Saiki, R.; Kaduwela, A.; Osterwalder, J.; Sagurton, M.; Fadley, C. S.; Brundle, C. R. *Journal of Vacuum Science & Technology A* **1987**, *5*, 932.

(40) Hall, R. B.; Chen, J. G.; Hardenbergh, J. H.; Mims, C. A. *Langmuir* **1991**, *7*, 2548.

(41) Kuhlenbeck, H.; Odörfer, G.; Jaeger, R.; Illing, G.; Menges, M.; Mull, T.; Freund, H. J.; Pöhlchen, M.; Staemmler, V.; Witzel, S.; Scharfschwerdt, C.; Wennemann, K.; Liedtke, T.; Neumann, M. *Physical Review B* **1991**, *43*, 1969.

(42) Stöhr, J.; Jaeger, R.; Kendelewicz, T. *Phys. Rev. Lett.* **1982**, *49*, 142.

(43) Pedio, M.; Becker, L.; Hillert, B.; D'Addato, S.; Haase, J. *Physical Review B* **1990**, *41*, 7462.

(44) Wang, S.-G.; Cao, D.-B.; Li, Y.-W.; Wang, J.; Jiao, H. *The Journal of Physical Chemistry B* **2005**, *109*, 18956.

(45) Conrad, H.; Ertl, G.; Küppers, J.; Latta, E. E. *Surface Science* **1976**, *57*, 475.

(46) Fleisch, T.; Winograd, N.; Delgass, W. N. *Surface Science* **1978**, *78*, 141.

(47) Oku, M.; Tokuda, H.; Hirokawa, K. *Journal of Electron Spectroscopy and Related Phenomena* **1991**, *53*, 201.

(48) Mansour, A. N. *Surface Science Spectra* **1994**, *3*, 231.

(49) Kitakatsu, N.; Maurice, V.; Marcus, P. *Surface Science* **1998**, *411*, 215.

(50) Holloway, P. H.; Hudson, J. B. *Journal of Vacuum Science & Technology* **1975**, *12*, 647.

(51) Eren, B.; Heine, C.; Bluhm, H.; Somorjai, G. A.; Salmeron, M. *Journal of the American Chemical Society* **2015**, *137*, 11186.

(52) Pantförder, J.; Pöllmann, S.; Zhu, J. F.; Borgmann, D.; Denecke, R.; Steinrück, H.-P. *Review of Scientific Instruments* **2005**, *76*, 014102.

(53) Óvári, L.; Krick Calderon, S.; Lykhach, Y.; Libuda, J.; Erdőhelyi, A.; Papp, C.; Kiss, J.; Steinrück, H. P. *Journal of Catalysis* **2013**, *307*, 132.

(54) Eichelbaum, M.; Hävecker, M.; Heine, C.; Wernbacher, A. M.; Rosowski, F.; Trunschke, A.; Schlögl, R. *Angewandte Chemie International Edition* **2015**, *54*, 2922.

(55) Jugnet, Y.; Loffreda, D.; Dupont, C.; Delbecq, F.; Ehret, E.; Cadete Santos Aires, F. J.; Mun, B. S.; Aksoy Akgul, F.; Liu, Z. *The Journal of Physical Chemistry Letters* **2012**, *3*, 3707.

(56) Axnanda, S.; Scheele, M.; Crumlin, E.; Mao, B.; Chang, R.; Rani, S.; Faiz, M.; Wang, S.; Alivisatos, A. P.; Liu, Z. *Nano Letters* **2013**, *13*, 6176.

(57) Roustila, A.; Severac, C.; Chêne, J.; Percheron-Guégan, A. *Surface Science* **1994**, *311*, 33.

(58) Nakamura, J.; Rodriguez, J. A.; Campbell, C. T. *Journal of Physics: Condensed Matter* **1989**, *1*, SB149.

(59) Mudiyanselage, K.; Senanayake, S. D.; Feria, L.; Kundu, S.; Baber, A. E.; Graciani, J.; Vidal, A. B.; Agnoli, S.; Evans, J.; Chang, R.; Axnanda, S.; Liu, Z.; Sanz, J. F.; Liu, P.; Rodriguez, J. A.; Stacchiola, D. J. *Angewandte Chemie International Edition* **2013**, *52*, 5101.

(60) Graciani, J.; Mudiyanselage, K.; Xu, F.; Baber, A. E.; Evans, J.; Senanayake, S. D.; Stacchiola, D. J.; Liu, P.; Hrbek, J.; Sanz, J. F.; Rodriguez, J. A. *Science* **2014**, *345*, 546.

(61) Urasaki, K.; Sekine, Y.; Kawabe, S.; Kikuchi, E.; Matsukata, M. *Applied Catalysis A: General* **2005**, *286*, 23.

(62) Weatherup, R. S.; D'Arsié, L.; Cabrero-Vilatela, A.; Caneva, S.; Blume, R.; Robertson, J.; Schloegl, R.; Hofmann, S. *Journal of the American Chemical Society* **2015**.

(63) Rostrup-Nielsen, J. R. *Journal of Catalysis* **1974**, *33*, 184.

(64) Monachino, E.; Greiner, M.; Knop-Gericke, A.; Schlögl, R.; Dri, C.; Vesselli, E.; Comelli, G. *The Journal of Physical Chemistry Letters* **2014**, *5*, 1929.

(65) Maglia, F.; Spinolo, G.; Anselmi-Tamburini, U. *Solid State Sciences* **2009**, *11*, 1686.

(66) Jang, W. L.; Lu, Y. M.; Hwang, W. S.; Dong, C. L.; Hsieh, P. H.; Chen, C. L.; Chan, T. S.; Lee, J. F. *EPL (Europhysics Letters)* **2011**, *96*, 37009.

(67) Ginsburg, J. M.; Piña, J.; El Solh, T.; de Lasa, H. I. *Industrial & Engineering Chemistry Research* **2005**, *44*, 4846.

(68) Sinharoy, S.; Levenson, L. L. *Thin Solid Films* **1978**, *53*, 31.

(69) Jacobson, P.; Stöger, B.; Garhofer, A.; Parkinson, G. S.; Schmid, M.; Caudillo, R.; Mittendorfer, F.; Redinger, J.; Diebold, U. *ACS Nano* **2012**, *6*, 3564.

(70) Chin, Y.-H.; Buda, C.; Neurock, M.; Iglesia, E. *Journal of the American Chemical Society* **2013**.

(71) Chen, C. S.; Lin, J. H.; You, J. H.; Yang, K. H. *The Journal of Physical Chemistry A* **2010**, *114*, 3773.

(72) Zhu, Z.; Butcher, D. R.; Mao, B.; Liu, Z.; Salmeron, M.; Somorjai, G. A. In *ABSTRACTS OF PAPERS OF THE AMERICAN CHEMICAL SOCIETY*; AMER CHEMICAL SOC 1155 16TH ST, NW, WASHINGTON, DC 20036 USA: 2013; Vol. 245.

(73) Over, H.; Kim, Y. D.; Seitsonen, A. P.; Wendt, S.; Lundgren, E.; Schmid, M.; Varga, P.; Morgante, A.; Ertl, G. *Science* **2000**, *287*, 1474.

(74) Chin, Y.-H.; Iglesia, E. *The Journal of Physical Chemistry C* **2011**, *115*, 17845.

(75) Sanchez Casalongue, H. G.; Ng, M. L.; Kaya, S.; Friebel, D.; Ogasawara, H.; Nilsson, A. *Angewandte Chemie International Edition* **2014**, *53*, 7169.

(76) Zhu, Z.; Melaet, G.; Axnanda, S.; Alayoglu, S.; Liu, Z.; Salmeron, M.; Somorjai, G. A. *Journal of the American Chemical Society* **2013**, *135*, 12560.

(77) Mark, M. F.; Maier, W. F. *Angewandte Chemie International Edition in English* **1994**, *33*, 1657.

(78) Grass, M. E.; Zhang, Y.; Butcher, D. R.; Park, J. Y.; Li, Y.; Bluhm, H.; Bratlie, K. M.; Zhang, T.; Somorjai, G. A. *Angewandte Chemie International Edition* **2008**, *47*, 8893.

(79) Navrotsky, A.; Ma, C.; Lilova, K.; Birkner, N. *Science* **2010**, *330*, 199.

(80) Merte, L. R.; Knudsen, J.; Eichhorn, F. M.; Porsgaard, S.; Zeuthen, H.; Grabow, L. C.; Lægsgaard, E.; Bluhm, H.; Salmeron, M.; Mavrikakis, M.; Besenbacher, F. *Journal of the American Chemical Society* **2011**, *133*, 10692.

(81) Melaet, G.; Ralston, W. T.; Li, C.-S.; Alayoglu, S.; An, K.; Musselwhite, N.; Kalkan, B.; Somorjai, G. A. *Journal of the American Chemical Society* **2014**, *136*, 2260.

(82) Mu, R.; Fu, Q.; Xu, H.; Zhang, H.; Huang, Y.; Jiang, Z.; Zhang, S.; Tan, D.; Bao, X. *Journal of the American Chemical Society* **2011**, *133*, 1978.

(83) Teschner, D.; Pestryakov, A.; Kleimenov, E.; Hävecker, M.; Bluhm, H.; Sauer, H.; Knop-Gericke, A.; Schlögl, R. *Journal of Catalysis* **2005**, *230*, 186.

(84) Gabasch, H.; Hayek, K.; Klötzer, B.; Unterberger, W.; Kleimenov, E.; Teschner, D.; Zafeiratos, S.; Hävecker, M.; Knop-Gericke, A.; Schlögl, R.; Aszalos-Kiss, B.; Zemlyanov, D. *The Journal of Physical Chemistry C* **2007**, *111*, 7957.

Table of Contents Graphic

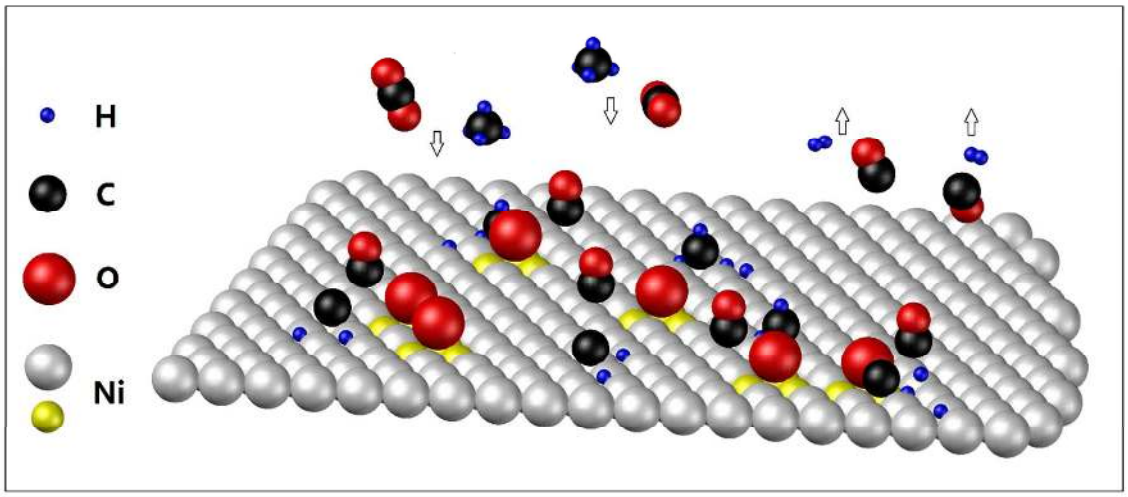

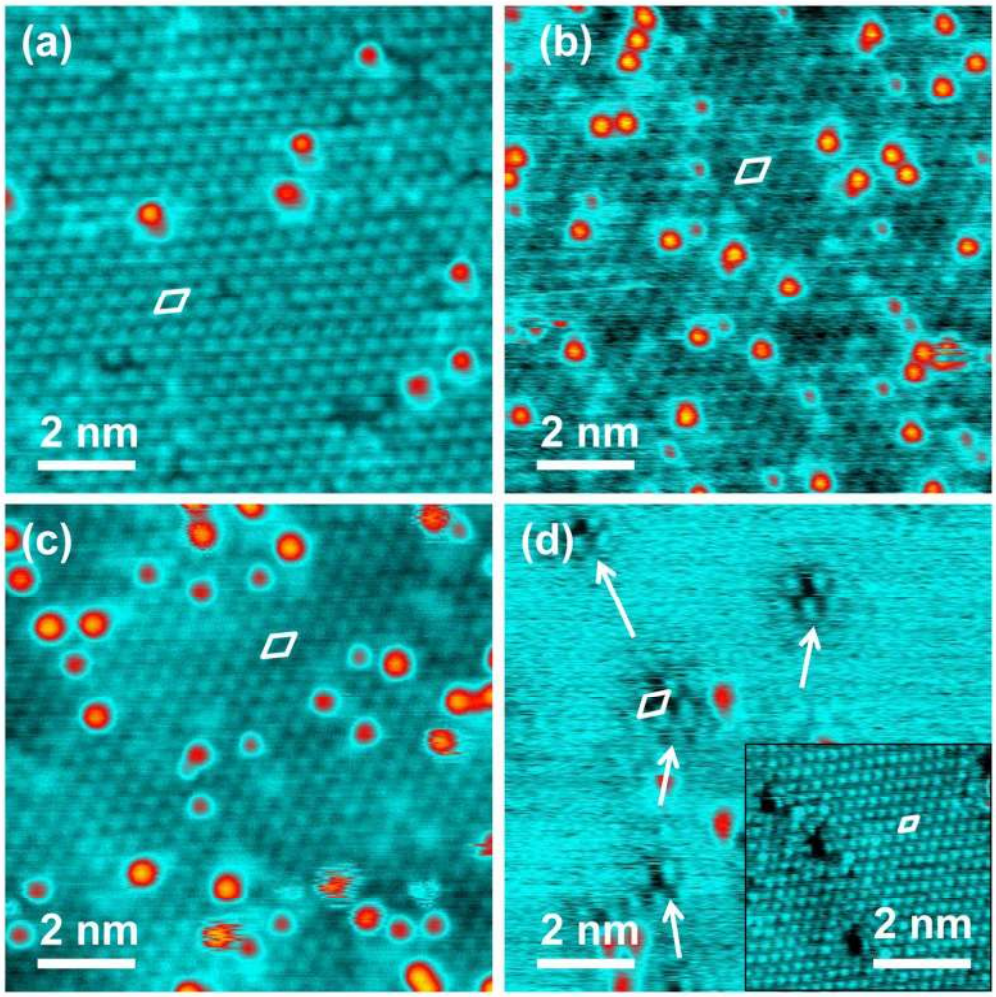

Figure 1. STM images of Ni-O(2×2) structures formed on Ni (111) after (a) exposing to 100 L CO_2 at room temperature; (b) after exposing to 100 L O_2 at RT followed by annealing at 773 K; (c) after exposing to 0.4 mbar CO_2 for 1 hour at 700 K, transferred in air, and cleaned by sputtering and annealing; and (d) after further annealing the sample corresponds to panel (c) at 973 K, leaving residual Chem-O islands dispersed on the flat surface [insert illustrates the same surface showing the Ni (111) lattice]. The unit cells were marked by diamonds, and measured as (a) 0.51±0.03 nm, (b) 0.49±0.04 nm, (c) 0.48±0.03 nm, (d) 0.49±0.04 nm for the residual islands, and 0.25±0.02 nm for the insert. The bias voltages and tunneling currents were (a) 0.2 V, 0.1 nA; (b) 0.05 V, 0.5 nA; (c) 0.2 V, 0.1 nA; (d) 0.1 V, 0.2 nA, and the insert 0.1 V, 10 nA.
119x119mm (300 x 300 DPI)

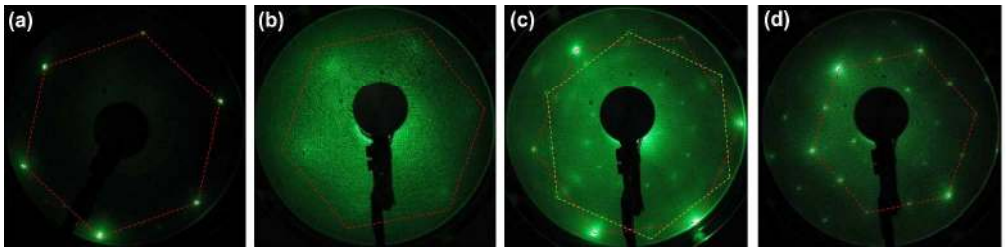

Figure 2. LEED patterns of (a) clean Ni (111), beam energy 70 eV; (b) after exposure to 0.4 mbar CO_2 at 600 K for 30 min, beam energy 70 eV, showing a shrinkage of the diffraction lattice consistent with epitaxial NiO (111) on Ni (111); and (c, d) the condition of (b) after UHV annealing, using 70 eV and 110 eV beams, showing the transition from NiO (111) to the p(2x2) Chem-O structure. The hexagons in red dashed lines denote the unit diffraction lattice of clean Ni (111), and that in yellow dashed lines denotes a rotated pattern.
617x149mm (300 x 300 DPI)

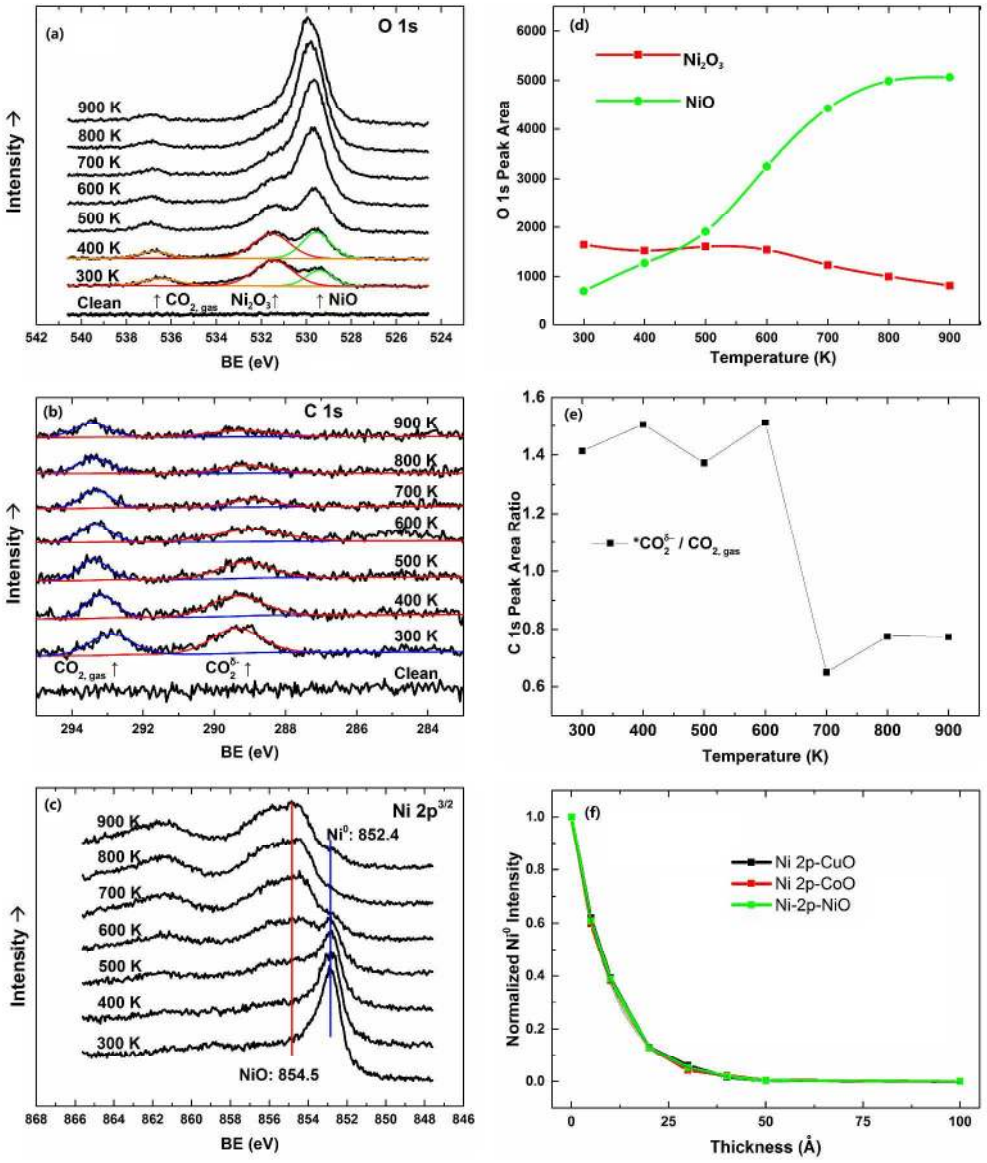

Figure 3. Temperature-programmed NAP-XPS under 0.4 mbar CO_2 from 300 K to 900 K. (a-c) O 1s, C 1s and Ni 2p $_{3/2}$ peaks. (d) Fitted O 1s areas by NiO (green) and Ni_2O_3 (red). (e) C 1s area ratio of $*CO_2^{\delta-}$ /$CO_{2,gas}$. (f) SESSA 2.0 simulated Ni^0 2p intensity (normalized) from nickel substrates covered by CuO, CoO, and NiO with varying thicknesses.
1481x1710mm (96 x 96 DPI)

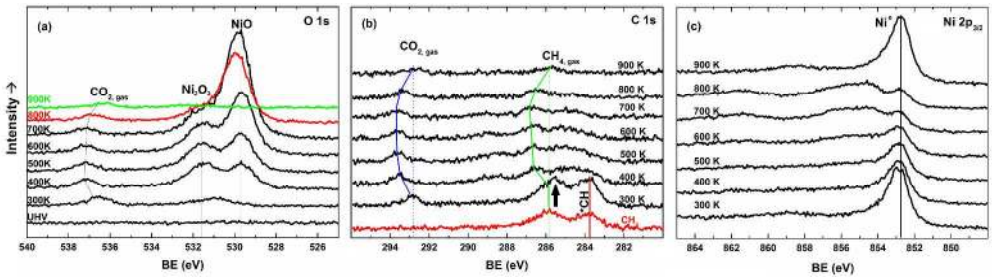

Figure 4. Temperature-programmed XP spectra of (a) O 1s, (b) C 1s and (c) Ni $2p_{3/2}$ under 0.4 mbar CH_4 and 0.4 mbar CO_2.
2036x556mm (96 x 96 DPI)

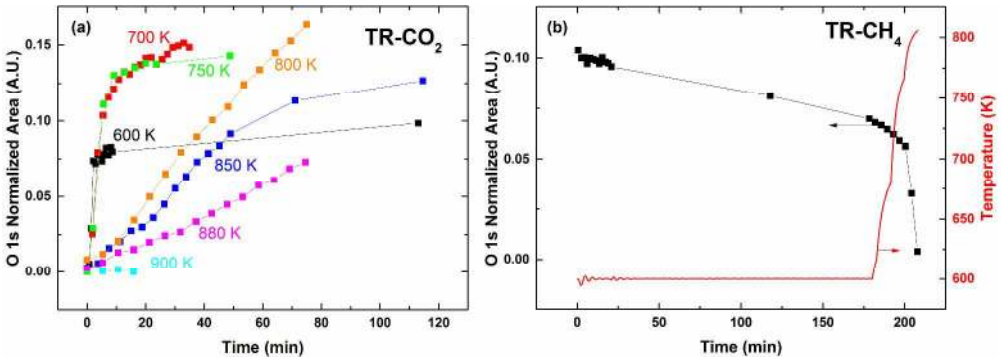

Figure 5. Time-resolved NAP-XPS showing the O 1s peak evolution. (a) Accumulation of oxygen under 0.4 mbar CO_2 at varying temperatures; (b) the reduction of the Ni-O phase under 0.3 mbar CH_4, prepared from the oxidation in (a) at 600 K.
1494x522mm (96 x 96 DPI)

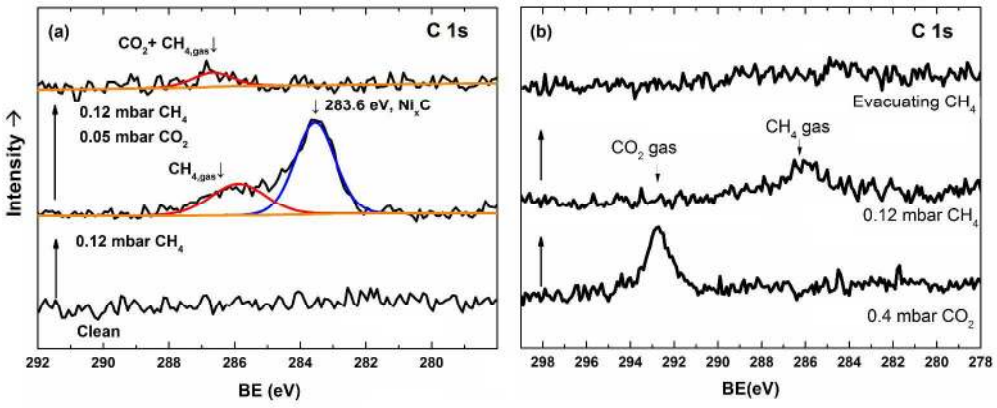

Figure 6. Titration experiments at 700 K with varying gas dosing sequences. In (a), the Ni (111) was first exposed to 0.12 mbar CH_4 at 700 K and Ni_xC clusters were formed; after adding another 0.05 mbar CO_2, the NixC phase disappeared. In (b), the Ni (111) was first exposed to 0.4 mbar CO_2 at 700 K to form a NiO surface; after evacuating the CO_2 and adding 0.12 mbar CH_4, no carbon deposition was observed on the oxidized surface except for the gas phase CH_4 peak, which disappeared after evacuating CH_4.
1380x560mm (96 x 96 DPI)

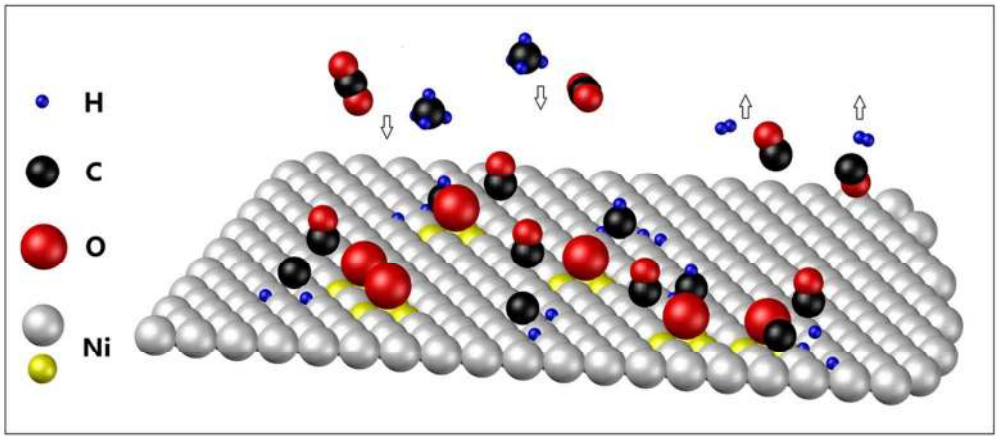

Table of Contents Graphic
98x43mm (300 x 300 DPI)